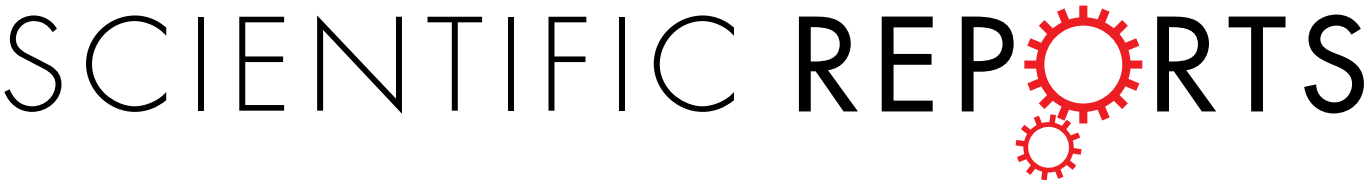

OPEN

Polarization-resolved and polarization- multiplexed spike encoding properties in photonic neuron based on VCSEL-SA

Received: 11 July 2018
Accepted: 18 October 2018
Published online: 31 October 2018

Yahui Zhang[1], Shuiying Xiang[1,2], Xingxing Guo[1], Aijun Wen[1] & Yue Hao[2]

The spike encoding properties of two polarization-resolved modes in vertical-cavity surface-emitting laser with an embedded saturable absorber (VCSEL-SA) are investigated numerically, based on the spin-flip model combined with the Yamada model. The results show that the external input optical pulse (EIOP) can be encoded into spikes in X-polarization (XP) mode, Y-polarization (YP) mode, or both XP and YP modes. Furthermore, the numerical bifurcation diagrams show that a lower (higher) strength of EIOP is beneficial for generating tonic (phasic) spikes; a small amplitude anisotropy contributes to wide (narrow) tonic spiking range in XP (YP) mode; a large current leads to low thresholds of EIOP strength for both XP and YP modes. However, the spike encoding properties are hardly affected by the phase anisotropy. The encoding rate is shown to be improved by increasing EIOP strength. Moreover, dual-channel polarization-multiplexed spike encoding can also be achieved in a single VCSEL-SA. To the best of our knowledge, such single channel polarization-resolved and dual-channel polarization-multiplexed spike encoding schemes have not yet been reported. Hence, this work is valuable for ultrafast photonic neuromorphic systems and brain-inspired information processing.

Vertical-cavity surface-emitting lasers (VCSELs) are popular candidates for many potential applications, including optical communication, optical signal processing, and optical computation, as they exhibit many advantages, such as low manufacturing cost, easy to integrate into two-dimensional arrays, and high energy efficiency[1,2]. In recent years, the nonlinear dynamics, polarization switching and polarization bistability properties of VCSELs have been intensively studied[3–14]. Interestingly, numerical and experimental investigations demonstrate that, by injecting external input optical pulse (EIOP), VCSELs can reproduce different behaviors exhibited by biological neurons including phasic spiking and tonic spiking, but on a much faster timescale[15–22]. Therefore, the VCSELs can be regarded as photonic neurons in the neuromorphic systems[18,20].

Compared with conventional VCSELs, the VCSEL with an embedded saturable absorber (VCSEL-SA) can offer the excitability threshold for photonic neuron[16,21]. Based on a two-section rate equation model derived from the well-known Yamada model, some representative cortical spiking algorithms have been demonstrated numerically in small circuits consisting of excitable VCSELs-SA, including multistable circuit, synfire chain, and spatiotemporal pattern recognition circuit[16]. In addition, our previous numerical findings indicate that the spike codes can be stored successfully in the mutually coupled VCSELs-SA system[21]. However, the effects of polarization dynamics of VCSEL-SA on the spiking properties are not addressed in these works.

Moreover, the previous works mainly focused on single-channel spike encoding in the photonic neurons[15–23]. For example, single-channel all-optical digital-to-spike conversion was realized in the photonic neuron based on graphene excitable laser[23]. Hence, it is still open to explore whether dual-channel spike encoding can be achieved in a single VCSEL-SA taking advantage of the polarization dynamics.

In this paper, we focus on the numerically realization of dual-channel spike encoding in VCSEL-SA, and concentrate on the effects of polarization dynamics on the spiking encoding. By combining the well-known spin-flip model (SFM) and the Yamada model, the spike encoding properties in two polarization-resolved modes, including X-polarization (XP) and Y-polarization (YP) modes of the VCSEL-SA are investigated numerically in

[1]State Key Laboratory of Integrated Service Networks, Xidian University, Xi'an, 710071, China. [2]State Key Discipline Laboratory of Wide Bandgap Semiconductor Technology, School of Microelectronics, Xidian University, Xi'an, 710071, China. Correspondence and requests for materials should be addressed to S.X. (email: jxxsy@126.com)

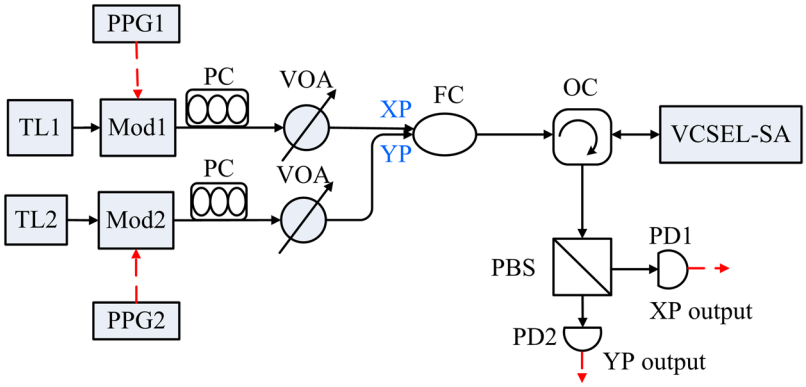

Figure 1. The schematic illustration of dual-channel spike encoding based on VCSEL-SA. TL1 and TL2: tunable laser; Mod1 and Mod2: modulator; PPG1 and PPG2: pulse signal generator; PC: polarization controller; VOA: variable optical attenuator; FC: fiber couple; OC: optical circulator; VCSEL-SA: vertical-cavity surface-emitting laser with an embedded saturable absorber; PBS: polarization beam splitter; PD1 and PD2: photodetector. The solid (dashed) lines correspond to optical (electrical) path.

detail. The roles of EIOP strength, amplitude anisotropy, phase anisotropy and two pump currents are considered. Furthermore, we explore the dual-channel polarization-multiplexed spiking encoding in a single VCSEL-SA for the first time.

Results

Model. The schematic diagram of dual-channel spike encoding based on VCSEL-SA is presented in Fig. 1. The output of TL1 (TL2) is considered as the optical input for XP (YP) mode. The pulses can be generated by PPG1 and PPG2. The polarization states of the two injected fields can be adjusted by PC. The output of FC is injected into the VCSEL-SA via OC. The VCSEL-SA device used in ref.[24], which is composed of two InGaAs/AlGaAs quantum wells for the gain section, and one InGaAs/AlGaAs quantum well for the SA section, can be employed in our proposed scheme. The two polarization-resolved modes of the VCSEL-SA are then separated via a PBS for achieving two channel outputs. In a possible experiment, the strength of EIOP can be easily controlled by VOA.

Formulation. The polarization dynamics of VCSEL can be described in the framework of the standard SFM[3,4]. The well-known Yamada model is successful for expressing a semiconductor laser with an embedded saturable absorber[16,21,25]. Our model is based on the combination of SFM and Yamada models[26,27]. We use two orthogonal linear components to replace two circularly polarized components as

$$F_x = \frac{F_+ + F_-}{\sqrt{2}},\ F_y = -\ i\frac{F_+ - F_-}{\sqrt{2}}. \tag{1}$$

By including the polarized EIOPs, the rate equations can be written as follows:

$$\frac{dF_x}{dt} = \frac{1}{2}(1 + i\alpha)[(D_1 + D_2 - 1)F_x + i(d_1 + d_2)F_y] - (\varepsilon_a + i\varepsilon_p)F_x + k_{injx}F_{injx}(t)e^{i\Delta\omega_x t} \tag{2}$$

$$\frac{dF_y}{dt} = \frac{1}{2}(1 + i\alpha)[(D_1 + D_2 - 1)F_y - i(d_1 + d_2)F_x] + (\varepsilon_a + i\varepsilon_p)F_y + k_{injy}F_{injy}(t)e^{i\Delta\omega_y t} \tag{3}$$

$$\begin{aligned} \dot{D_{1,2}} &= \gamma_{1,2}[\mu_{1,2} - D_{1,2} - \frac{1}{2}a_{1,2}(D_{1,2} + d_{1,2})|F_x - iF_y|^2 \\ &\quad - \frac{1}{2}a_{1,2}(D_{1,2} - d_{1,2})|F_x + iF_y|^2 + c_{12,21}D_{2,1}] \end{aligned} \tag{4}$$

$$\begin{aligned} \dot{d_{1,2}} &= -\gamma_{s1,2}d_{1,2} - \gamma_{1,2}[\frac{1}{2}a_{1,2}(D_{1,2} + d_{1,2})|F_x - iF_y|^2 \\ &\quad - \frac{1}{2}a_{1,2}(D_{1,2} - d_{1,2})|F_x + iF_y|^2 - c_{12,21}d_{2,1}] \end{aligned} \tag{5}$$

where the subscripts 1 and 2 represent the pump and absorbing regions, respectively. $F_{x,y}$ represent the slowly varying complex amplitudes of the two linear polarized components of the electric field. $D_{1,2}$ represent the total carrier inversion between the conduction and valence bands related to the transparency carrier density. $d_{1,2}$ represent the carrier inversions with opposite spin orientations. ε_a (ε_p) is the amplitude (phase) anisotropy. The terms $k_{injx,y}F_{injx,y}(t)e^{i\Delta\omega_{x,y}t}$ in Eqs (2) and (3) denote the EIOPs, where $k_{injx,y}$ are the input strength, $F_{injx,y}$ characterize the

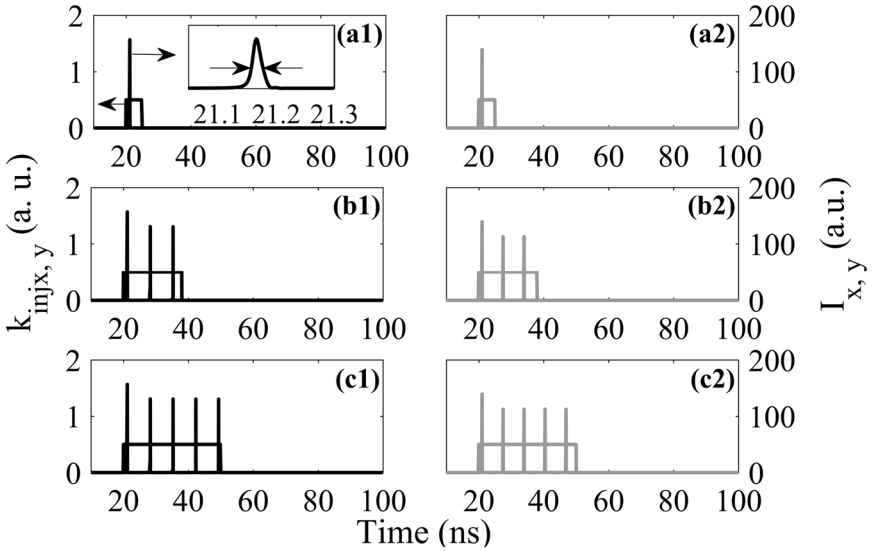

Figure 2. The polarization-resolved responses of VCSEL-SA subject to EIOP. (**a1**)–(**c1**) correspond to the case (i) with the during time 5 ns, 18 ns and 30 ns respectively. (**a2**)–(**c2**) correspond to the case (ii) with the during time 5 ns, 18 ns and 30 ns, respectively. The inset in (**a1**) indicates an enlargement of the generated spike.

optical pulse injection, and $\Delta\omega_{x,y}$ is the angular frequency detuning between the injecting field and the VCSEL-SA. The terms $c_{12}D_2$ and $c_{21}D_1$ are the carrier diffusion. α is the linewidth enhancement factor, $\mu_{1,2}$ are the injection currents, $\gamma_{1,2}$ are the total carrier decay rates, and $\gamma_{s1,2}$ are the effective spin-flip rates. $a_{1,2}$ are the differential gains. Here, we define $\varepsilon_p = \gamma_p/\kappa$, where γ_p denotes the birefringence, and κ is the cavity decay rate. The equations are written in a dimensionless form so the time is measured in units of κ^{-1}. The following parameters are used in simulation[26,27]: $\alpha = 3$, $\mu_1 = 2.1$, $\mu_2 = -6.1$, $\gamma_1 = 1.09 \times 10^{-3}$, $\gamma_2 = 1.13 \times 10^{-3}$, $\gamma_{s1} = \gamma_{s2} = 0.25$, $\varepsilon_a = 0$, $\gamma_p = 15\, ns^{-1}$, $\kappa = 390\, ns^{-1}$, $\Delta\omega_{x,y} = 0\, rad/s$, $a_1 = 1$, $a_2 = 8.7$, $c_{12} = 2.84 \times 10^{-2}$, $c_{21} = 1.91$. With these parameters, the VCSEL-SA operates right below the lasing threshold $\mu_{th} = 2.6$. Thus, without any external optical injection, no laser light is emitted[24].

Single-channel polarization-resolved spike encoding. In this section, we first consider polarization-resolved spike encoding in VCSEL-SA for two injection cases, (i) the EIOP is injected in XP mode, i.e., $k_{injx} \neq 0$, $k_{injy} = 0$; (ii) the EIOP is injected in YP mode, i.e., $k_{injx} = 0$, $k_{injy} \neq 0$. Then, the effects of EIOP strength, amplitude anisotropy, phase anisotropy and pump currents are studied. The distribution of time intervals between the encoding spikes is investigated.

Figure 2 indicates the responses of the polarization-resolved modes in VCSEL-SA subject to EIOPs. Here, three different temporal durations (denoted as $\Delta\tau$) are considered for both injection cases. The shape of the EIOP is rectangular with $k_{injx,y} = 0.5$. The output intensities are denoted as $I_x = |F_x|^2$ and $I_y = |F_y|^2$, respectively. It can be seen from Fig. 2(a1) that, for case (i), when $\Delta\tau = 5$ ns, one spike is responded in XP mode. Note that, the solitary VCSEL-SA operates right below its lasing threshold, and the EIOP brings the laser above the threshold and triggers the firing of spikes. The full width at half maximum (FWHM) of the generated spike is denoted as τ_{FWHM}, and is $\tau_{FWHM} = 17\, ps$ as shown in the inset of Fig. 2(a1). For $\Delta\tau = 18$ ps ($\Delta\tau = 30$ ps), it can be seen from Fig. 2(b1),(c1), three (five) spikes are obtained in the XP mode. Furthermore, the value of τ_{FWHM} is the same as that in Fig. 2(a1). As can be seen in Fig. 2(a2)–(c2), for case (ii), with different $\Delta\tau$ of EIOP, the EIOP is encoded into one, three, and five spikes in YP mode, respectively, which are similar to the responses in XP mode. The τ_{FWHM} is also 17 ps. That is to say, the EIOP can be successfully encoded into spikes in two polarization-resolved modes, respectively. Besides, a large $\Delta\tau$ leads to more spikes in the polarization-resolved modes for both injection cases, while the FWHM of the generated spikes is hardly affected by $\Delta\tau$.

Next, the effect of EIOP strength on the spiking encoding in the polarization-resolved modes is studied. As the response properties in YP mode are similar to those in XP mode, we only present the spike encoding properties in XP mode for simplicity. The responses in XP mode of VCSEL-SA for different EIOP strengths are presented in Fig. 3(a)–(f). Here, we consider $\Delta\tau = 70$ ns. It can be seen from Fig. 3(a), when $k_{injx} = 0.25$, no spike is generated, indicating that the strength is below the excitability threshold. From Fig. 3(b)–(d), we can see that, when $k_{injx} = 0.28$, 0.4 and 0.6, the responses of VCSEL-SA during the EIOP are multiple periodic spikes, and the corresponding τ_{FWHM} is 19 ps, 18 ps and 17 ps, respectively. Interestingly, such multiple periodic spikes are similar to the tonic spiking obtained experimentally and numerically based on the SFM in conventional VCSEL[15,17]. Moreover, the intervals between two consecutive spikes decrease with the increase of k_{injx}. Also, the intensity of the first spike is increased with the increasing k_{injx}. The response for $k_{injx} = 0.75$ is presented in Fig. 3(e), the output consists of one large intensity spike (with $\tau_{FWHM} = 16$ ps) and some damped spikes. Eventually, the intensity is about 1 in the remaining duration of the EIOP, as shown in the inset. When the k_{injx} is further increased, only one large intensity spike (with $\tau_{FWHM} = 15$ ps) is generated in XP mode upon the arrival of EIOP as shown in Fig. 3(f)

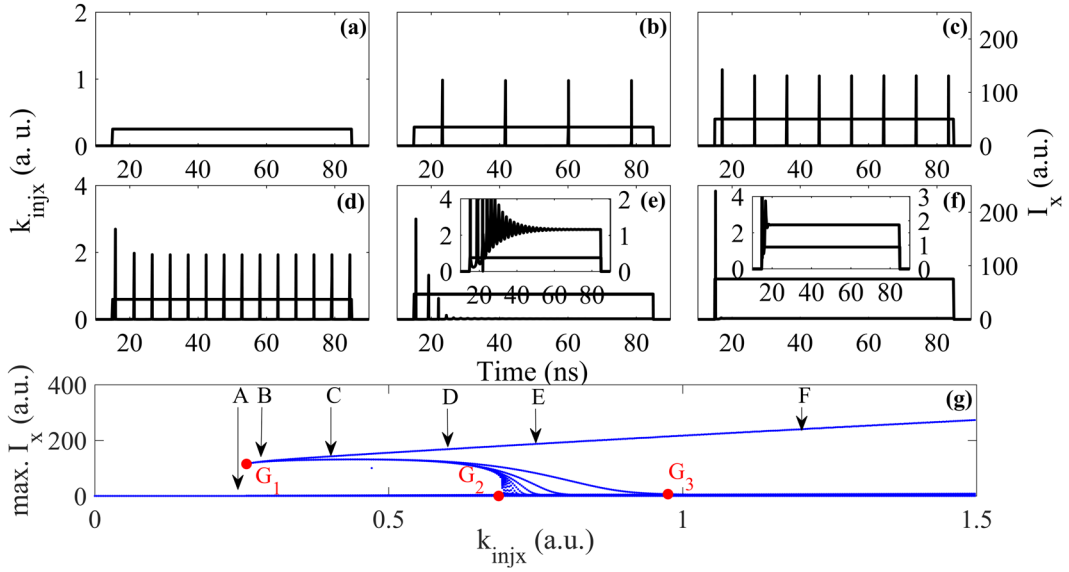

Figure 3. The responses of VCSEL-SA to EIOP subject XP mode (**a**)–(**f**) and the numerical bifurcation diagram of XP mode as a function of k_{injx} (**g**). (**a**)–(**f**) with $k_{injx} = 0.25, 0.28, 0.4, 0.6, 0.75, 1.2$. The enlargements of the generated spikes of (**e**),(**f**) are plotted in the insets.

for $k_{injx} = 1.2$, which is similar to the phasic spiking reported in conventional VCSEL[15,17]. It also can be seen from the inset, the intensity is about 2 in the remaining duration of the EIOP. Note that, the stable states shown in Fig. 3(e) and (f), originate from the injection-locking effect. That is to say, the large intensity spike is the result of a transitory effect produced by switching transitions between the non-lasing state and the injection locking state[15].

It has already been shown that, the bifurcation diagram is a useful tool to characterize different neuron-like dynamics[20,22]. The phasic spiking and tonic spiking have been identified in conventional VCSEL[20]. We also present the bifurcation diagram, i.e., the maximum of I_x as a function of k_{injx}, in Fig. 3(g). It can be found that, the excitability threshold is $k_{injx} = 0.26$, corresponding to the red dot G_1. When $k_{injx} < 0.26$, no spike is generated, corresponding to the response shown in Fig. 3(a) for $k_{injx} = 0.25$ shown by arrow A. When $0.26 < k_{injx} < 0.69$ (red dot G_2), for the pointed arrows B, C and D corresponding to the k_{injx} used in Fig. 3(b)–(d), tonic spiking is obtained. When $0.69 < k_{injx} < 0.98$ (red dot G_3), a large intensity spike followed by damped spikes is observed, a representative case is shown in Fig. 3(e), shown by the arrow E corresponding to the $k_{injx} = 0.75$. When $k_{injx} < 0.98$, phasic spiking is obtained, which can be seen clearly from Fig. 3(f) corresponding to arrow F.

Next, we use the bifurcation diagram to further analyze the effect of different parameters on spiking coding characteristics. Figure 4 presents the bifurcation diagram for the response as a function of $k_{injx,y}$ under different cases of amplitude anisotropy, phase anisotropy and injection currents. The other parameters are identical to those in Fig. 3(g). For injection case (i), bifurcation diagrams for XP mode as a function of k_{injx} under different amplitude anisotropy ε_a are presented in Fig. 4(a1)–(a4). It can be seen that, the excitability threshold is approximately $k_{injx} = 0.26$ for all different cases of ε_a. Besides, the range of k_{injx} corresponding to tonic spiking is $0.26 < k_{injx} < 0.74$, for $\varepsilon_a = -0.1$, $0.26 < k_{injx} < 0.72$ for $\varepsilon_a = -0.05$, $0.26 < k_{injx} < 0.66$ for $\varepsilon_a = 0.05$ and $0.27 < k_{injx} < 0.62$ for $\varepsilon_a = 0.1$. In addition, the range of k_{injx} corresponding to phasic spiking is $k_{injx} > 1.06$ for $\varepsilon_a = -0.1$, $k_{injx} > 1.05$ for $\varepsilon_a = -0.05$, $k_{injx} > 0.94$ for $\varepsilon_a = -0.05$ and $k_{injx} > 0.84$ for $\varepsilon_a = 0.1$. Namely, for a larger ε_a, the range of k_{injx} corresponding to tonic spiking is narrower, and the minimum k_{injx} corresponding to the onset of phasic spiking moves to a lower value. Correspondingly, for injection case (ii), the bifurcation diagrams for YP mode as a function of k_{injy} under different ε_a are presented in Fig. 4(b1)–(b4). It can be seen that, when $\varepsilon_a = -0.1$, -0.05, 0.05 and 0.1, the ranges of k_{injy} corresponding to the tonic spiking are $0.24 < k_{injx} < 0.66$, $0.24 < k_{injx} < 0.67$, $0.24 < k_{injx} < 0.72$, and $0.23 < k_{injx} < 0.77$, respectively. Additionally, the minimum value of k_{injy} corresponding to the onset of phasic spiking is 0.81, 0.89, 1.06 and 1.14, respectively. That is to say, the excitability threshold is also approximately the same for different ε_a in YP mode. Besides, the range of k_{injy} corresponding to tonic spiking is broadened for a larger ε_a, while the minimum k_{injy} corresponding to the onset of phasic spiking moves to higher value, which contrasts with the injection case (i). The numerical bifurcation diagrams for different ε_p are shown in Fig. 4(c1)–(c4) for injection case (i). It can be seen that, the four bifurcation diagrams are similar, and are also identical to Fig. 3(g). That is to say, the spike encoding property is hardly affected by ε_p. The bifurcation diagrams for injection case (i) under different μ_1 are presented in Fig. 4(d1)–(d4). It can be seen that, a larger μ_1 leads to a lower excitability threshold. More precisely, the value of excitability threshold is 0.44, 0.35, 0.17 and 0.11 for $\mu_1 = 1.9$, 2.0, 2.2 and 2.3, respectively. Besides, a larger μ_1 contributes to a wider range of k_{injx} corresponding to tonic spiking. In addition, the k_{injx} corresponding to the end of tonic spiking is 0.73, 0.71, 0.67 and 0.65 for $\mu_1 = 1.9$, 2.0, 2.2 and 2.3, respectively. Note that, the minimum values of k_{injx} corresponding to the onset of phasic spiking are almost similar for different cases of μ_1. The bifurcation diagrams for different μ_2 are presented in Fig. 4(e1)–(e4) for injection case (i). It can be seen that, the value of excitability threshold is 0.16, 0.21, 0.32 and 0.38 for $\mu_2 = -5.7$, -5.9, -6.3 and -6.5, respectively, indicating that a larger μ_2 also leads to a lower excitability

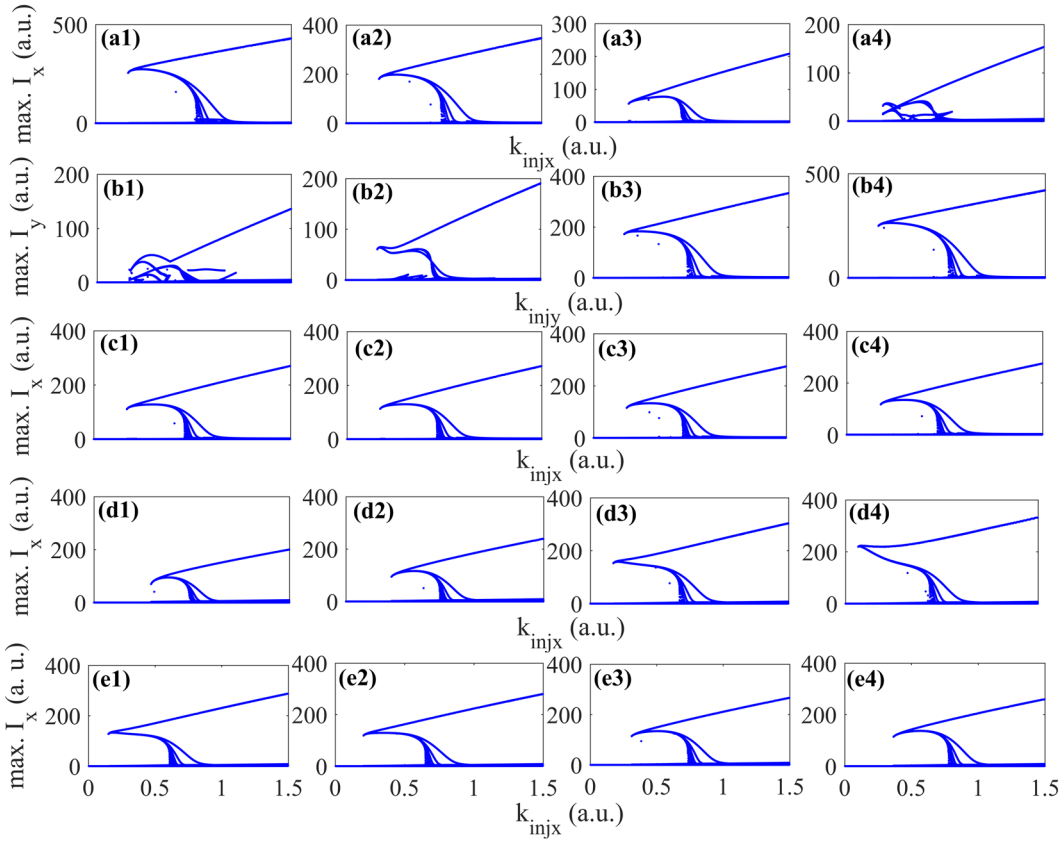

Figure 4. Numberical bifurcation diagrams as a function of k_{injx} under different cases of ε_a in XP mode (**a1**)–(**a4**), ε_a in YP mode (**b1**)–(**b4**), ε_p in XP mode (**c1**)–(**c4**), μ_1 in XP mode (**d1**)–(**d4**) and μ_2 in XP mode (**e1**)–(**e4**). (**a1**)–(**a4**), (**b1**)–(**b4**) corresponding to $\varepsilon_a = -0.1$, -0.05, 0.05 and 0.1, (**c1**)–(**c4**) corresponding to $\gamma_p = 9$, 12, 18 and 21 ns^{-1}, (**d1**)–(**d4**) corresponding to $\mu_1 = 1.9$, 2.0, 2.2 and 2.3, (**e1**)–(**e4**) corresponding to $\mu_2 = -5.7$, -5.9, -6.3 and -6.5.

threshold. Besides, the ranges of k_{injx} corresponding to tonic spiking are almost similar for different cases of μ_2. The k_{injx} corresponding to the end of tonic spiking is 0.60, 0.65, 0.74 and 0.77 for $\mu_2 = -5.7$, -5.9, -6.3 and -6.5, respectively. In addition, the minimum k_{injx} corresponding to the onset of phasic spiking is 0.89, 0.94, 1.05 and 1.06 for $\mu_2 = -5.7$, -5.9, -6.3 and -6.5, respectively. The bifurcation diagrams of YP mode for injection case (ii) are similar to those of XP mode for different cases of ε_p, μ_1, and μ_2, and are not shown here.

The time interval between the onset of EIOP and the first output spike (denoted as Δt_1[21]) and the time interval between two consecutive output spikes (denoted as Δt_2[21]) as functions of k_{injx} (k_{injy}) for both injection cases are presented in Fig. 5. Here, we also consider $\Delta\tau = 70$ ns. On the one hand, for injection case (i), it can be seen from Fig. 5(a) that, with the increase of k_{injx}, the values of Δt_1 decrease sharply and then converge, while the values of Δt_2 decrease sharply and then disappear when $k_{injx} > 0.88$. The values of Δt_1 are close to 0.27 ns when k_{injx} approach 1. For clarity, the values of Δt_1 and Δt_2 versus k_{injx} are also presented in log-log plots as shown in the inset. Moreover, we find that, the value of Δt_2 is always greater than 2 ns (blue dashed line). Hence, the $\Delta\tau$ can be fixed at 2 ns to ensure a single spike output for a given EIOP. Note, the k_{injx} should be large enough and above the excitability threshold, that is, $k_{injx} = 0.41$ for $\Delta\tau = 2$ ns. On the other hand, it can be seen in Fig. 5(b) that, similar results are found for injection case (ii). In this way, temporal spike encoding based on the spike latency, i.e., Δt_1, can be achieved in the VCSEL-SA[28,29].

Next, we further discuss the encoding rate, which is closely related to the refractory period of a photonic neuron[23]. For simplicity, the return-to-zero (RZ) sequence, whose period is denoted as ΔT, is regarded as EIOP. Here, ten bits of 1 are considered, and the pulse width in one bit is fixed at 2 ns. In this way, the successful one-bit-to-one-spike encoding is identified by ten spikes in the response. For convenience, a successful spike is characterized by max. $I_{x,y} \geq 20$ in the given bit duration. On the one hand, for injection case (i), the output spike numbers as functions of ΔT for four different k_{injx} are presented in Fig. 6(a1). It can be seen that, the spike number increases step-wise with the increase of ΔT and finally reaches ten at $\Delta T = 12.2$ ns for $k_{injx} = 0.45$, at $\Delta T = 7.6$ ns for $k_{injx} = 0.6$, at $\Delta T = 6$ ns for $k_{injx} = 0.7$ and at $\Delta T = 3$ ns for $k_{injx} = 1.3$, respectively. That is to say, the ten bits can be encoded correctly in the XP mode only when ΔT is sufficiently large, which can be attributed to the refractory period[28,29]. Besides, for a larger k_{injx}, the output spike number reaches ten at a smaller ΔT. Thus, the encoding rate, which is equal to $1/\Delta T$, can be improved by increasing k_{injx}. Usually, the encoding rate can be further improved by decreasing the volumes of the cavities and material recombination times[24]. On the other hand, for injection case (ii), the output spike numbers as functions of ΔT for four different k_{injy} are presented in Fig. 6(b1). We can

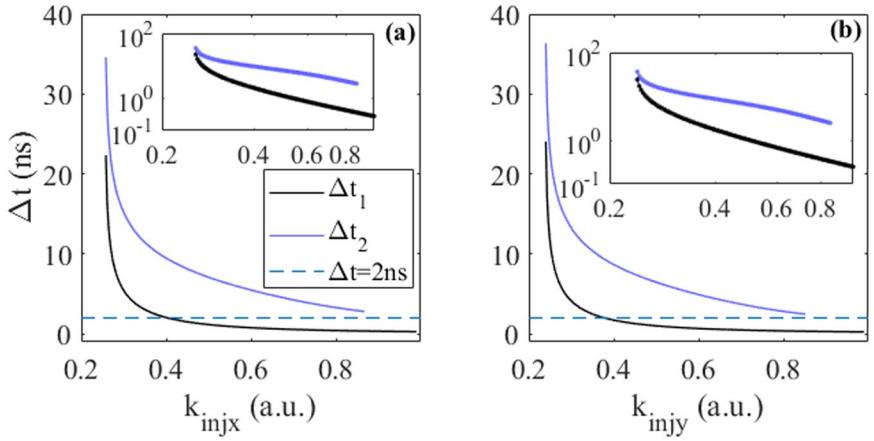

Figure 5. Δt_1 (black solid line) and Δt_2 (purple solid line) as functions of k_{injx} under XP mode (**a**) and k_{injy} under YP mode (**b**). The dashed blue line represent $\Delta t = 2$ ns. The insets are the corresponding log-log plots.

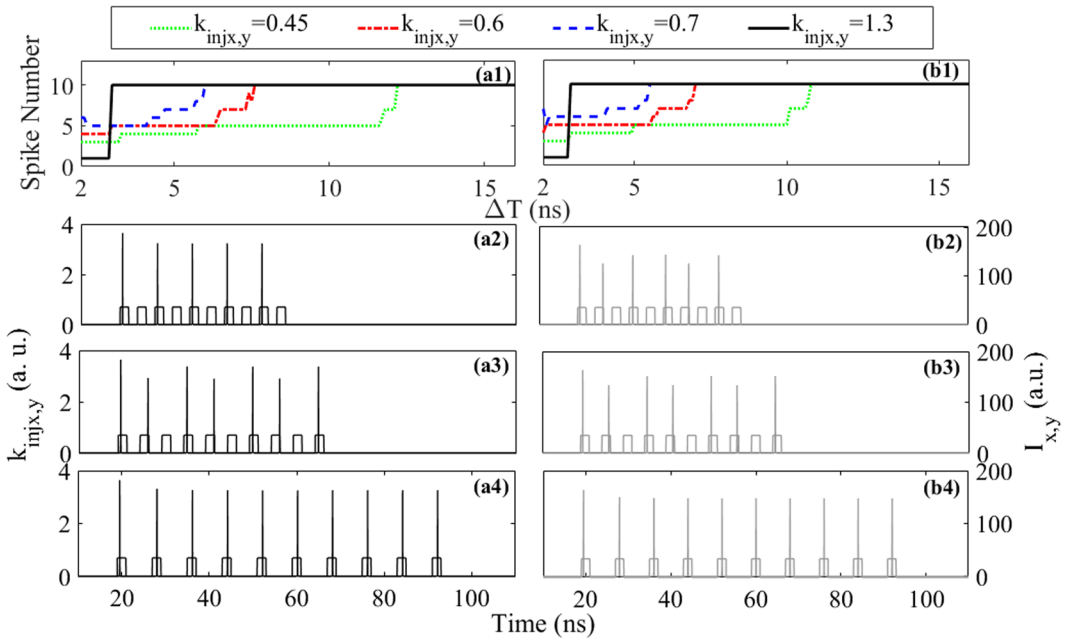

Figure 6. The spike number as functions of bit period ΔT (**a1**) for XP mode and (**b1**) YP mode. The time series of responses (**a2**)–(**a4**) in the XP mode and (**b2**)–(**b4**) YP mode, with $\Delta T = 4$ ns in (**a2**) and (**b2**), $\Delta T = 5$ ns in (**a3**) and (**b3**), and $\Delta T = 8$ ns in (**a4**) and (**b4**).

find that, the minimum ΔT corresponding to ten spikes is $\Delta T = 10.8$ ns for $k_{injy} = 0.45$, $\Delta T = 7$ ns for $k_{injy} = 0.6$, $\Delta T = 5.5$ ns for $k_{injy} = 0.7$ and $\Delta T = 2.9$ ns for $k_{injy} = 1.3$, respectively. Namely, the ten bits can also be encoded correctly in YP mode for sufficiently large ΔT, and higher encoding rate can be achieved for larger k_{injy}. In order to intuitively present the encoding process, the time series of responses in the XP mode for three representative ΔT are presented in Fig. 6(a2)–(a4) with $k_{injx} = 0.7$. It can be clearly seen that, ten bits are encoded into five spikes for $\Delta T = 4$ ns, and seven spikes for $\Delta T = 5$ ns. Namely, the one-bit-to-one-spike encoding fails due to the refractory period. For $\Delta T = 8$ ns, ten bits are successfully encoded into ten spikes. Correspondingly, the time series of responses in the YP mode for three representative cases of ΔT are presented in Fig. 6(b2)–(b4), and similar results are obtained.

Dual-channel polarization-multiplexed spike encoding. Next, we explore the polarization-multiplexed spike encoding in a single VCSEL-SA. That is to say, two different EIOPs are injected in both XP and YP modes, respectively, i.e., $k_{injx} \neq 0$, $k_{injy} \neq 0$. Through extensive calculation, we find that when k_{injx} and k_{injy} are relative small, the polarization mode competition and multiple polarization switching will occur and seriously affect the tonic spiking dynamics, leading to very complex spike encoding properties. Hence, for simplicity, we only consider large values of k_{injx} and k_{injy} corresponding to phasic spiking dynamics. The responses in both XP and YP modes for four representative

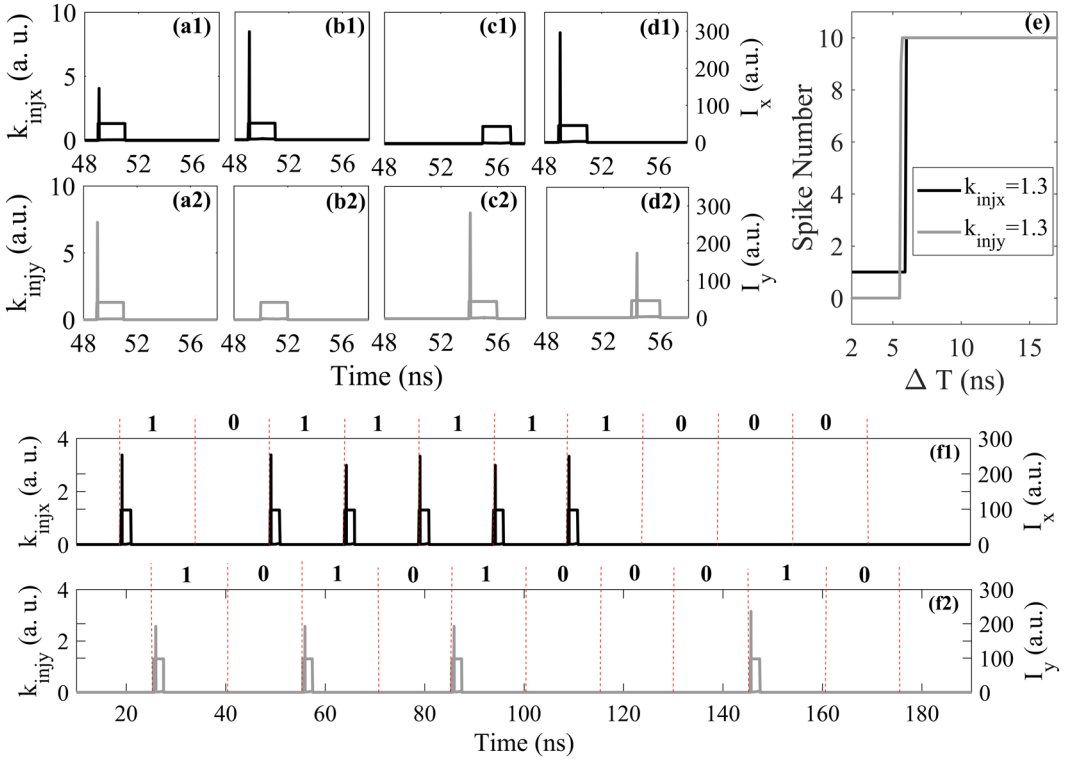

Figure 7. The response outputs of VCSEL-SA subject to two EIOPs for four representative cases. (**a**) the time windows of EIOPs are completely overlapped, (**b**) the EIOP injected into XP arrives earlier,(**c**) the EIOP injected into YP arrives earlier, (**d**) two EIOPs are well separated. (**e**) Spike numbers as functions of ΔT for $k_{injx} = 1.3$ and $k_{injy} = 1.3$. The response outputs of VCSEL-SA subject to pseudo-random bit sequences in XP (**f1**) and YP (**f2**) mode for ΔT = 15 ns.

cases are shown in Fig. 7. Here, we consider $\Delta\tau = 70$ ns, $k_{injx} = 1.3$ and $k_{injy} = 1.3$. It can be seen that, when the time windows of EIOPs are completely overlapped as shown in Fig. 7(a1) and (a2), the phasic spike is responded shortly after the arrival of EIOPs in both XP and YP modes. In this case, the EIOPs arrive simultaneously, hence both XP and YP mode share the carriers in VCSEL-SA. However, when the time windows of two EIOPs are partially overlapped, as can be seen in Fig. 7(b1),(b2),(c1) and (c2), the phasic spike can only be achieved in the XP (YP) mode when the EIOP received by the XP (YP) mode is arrived earlier. Note that, the spike triggered by the earlier arrival leads to carrier depletion via polarization mode competition[7,10]. The threshold cannot be reached to trigger another spike in the other mode. Interestingly, such behavior is quite similar to a biological behavior of an inhibitory interneuron that hinders the firing of others[30]. As presented in Fig. 7(d1) and (d2), the phasic spikes can also be generated successfully in both XP and YP modes when the two EIOPs are well separated. We have also discussed the encoding rate for the polarization-multiplexed spike encoding. To ensure successful dual-channel polarization-multiplexed spike encoding in a single VCSEL-SA, two sequences with half-period difference are injected into both XP and YP modes. The output spike numbers in XP and YP modes as functions of ΔT are further presented in Fig. 7(e). Here, a representative case of $k_{injx} = 1.3$, $k_{injy} = 1.3$ is considered. It can be seen that, when ΔT > 6 ns (ΔT > 5.7 ns), ten spikes can be generated in XP (YP) mode. Hence dual-channel polarization-multiplexed spike encoding can be achieved in a single VCSEL-SA when ΔT > 6 ns. Besides, to obtain more general results, we also consider the pseudo-random bit sequence as the EIOP. Here, the response outputs for only one representative ΔT is presented. It can be seen from Fig. 7(f1) and (f2) that, ten bits of pseudo-random sequence are encoded successfully in both XP and YP mode for $k_{injx} = 1.3$ and $k_{injy} = 1.3$. Note that, the polarization-multiplexed spike encoding scheme guarantees dual-channel parallel information processing in a single VCSEL-SA, which leads to reduced system cost. Hence, it is valuable for the implementation of parallel photonic information processing and photonic neuromorphic systems. Moreover, the polarization-multiplexed spike encoding may also be interesting for two channel vector coding[31].

Robustness to noise. Without loss of generality, we also consider the effect of signal noise on the spike encoding properties. Here, white Gaussian noise is added to the RZ sequences[23]. The encoding outputs for different signal-to-noise ratios (SNR) are presented in Fig. 8 for three injection cases mentioned above. To ensure the successful spike encoding for all the injection cases, we select ΔT = 60 ns, $k_{injx} = 0.7$ and $k_{injy} = 0.7$. It can be seen from Fig. 8(a1),(a2),(b1) and (b2) that, for both SNR = 30 dB and SNR = 20 dB, two spikes can be generated in XP or YP modes in VCSEL-SA. Moreover, for both cases of SNR, two spikes can be achieved in a single VCSEL-SA by polarization-multiplexed spike encoding. Hence, the polarization-resolved and polarization-multiplexed spike encoding schemes in VCSEL-SA are robust to noisy RZ sequences, which is similar to the finding obtained in a graphene excitable laser[23]. The white Gaussian noises induced timing jitters of output spikes are presented in the

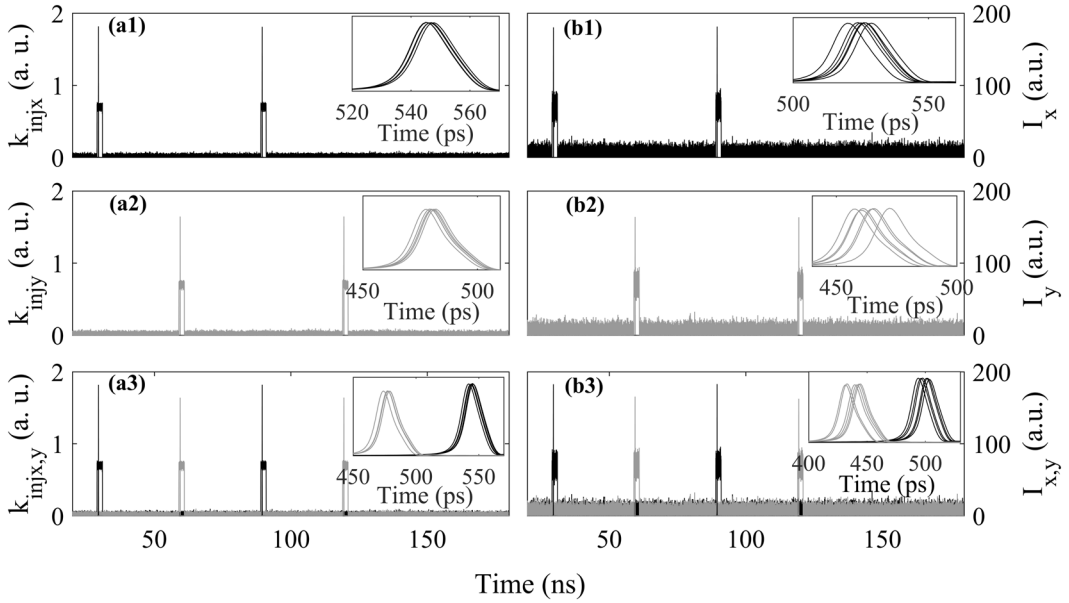

Figure 8. Numerical simulation of RZ bit sequence encoding in XP mode ((**a1**) and (**b1**)), YP mode ((**a2**) and (**b2**)), and both in XP and YP modes ((**a3**) and (**b3**)), when the RZ bit sequence has an SNR = 30 dB ((**a1**)–(**a3**)), SNR = 20 dB ((**b1**)–(**b3**)). Insets: eye diagrams corresponding to (**a1**)–(**b3**), respectively.

insets in Fig. 8(a1)–(a3) by eye diagrams[23] of six spikes. It can be seen that, the timing jitter[23] is about 2 ps (9 ps) for SNR = 30 dB (20 dB). Compared to the values of Δt_1 and Δt_2 shown in Fig. 5, the timing jitters are small and negligible. Hence, in temporal coding process, the timing jitter can be neglected by properly selecting the EIOP strength.

Discussion

In the present work, we derive the theoretical model to account for the polarization dynamics, saturable absorber, and EIOP in VCSEL-SA, by combing the well-known SFM and Yamada models. The single-channel spike encoding in the polarization-resolved modes and the dual-channel polarization-multiplexed spike encoding in a single VCSEL-SA are investigated numerically. The results show that the EIOPs can be encoded into spikes in XP mode, YP mode, or both XP and YP mode in VCSEL-SA. Besides, the generated spikes are similar to the tonic spiking and phasic spiking observed in traditional VCSEL. In addition, the numerical bifurcation analyses indicate that a small value of EIOP strength is beneficial for generating tonic spiking; a large value of EIOP strength is beneficial for generating phasic spiking; a small amplitude anisotropy contributes to a wide (narrow) range of tonic spiking in XP (YP) mode; large pump currents lead to low excitability threshold. While the spike encoding properties are hardly affected by the phase anisotropy. In the context of single-channel spike encoding, the encoding rate can be improved by increasing input strength. Furthermore, the polarization-multiplexed spike encoding is achieved in a single VCSEL-SA under proper condition. At last, we find that the polarization-resolved spike encoding as well as the polarization-multiplexed spike encoding are robust to noisy RZ sequences. To the best of our knowledge, such polarization-resolved and polarization-multiplexed spike encoding have not yet been reported, and are interesting and valuable for the ultrafast photonic neuromorphic systems and brain-inspired photonic information processing.

Methods

The Eqs (2)–(5) for VCSEL-SA are simulated in the MATLAB platform. They have been integrated by using a fourth-order Runge-Kutta algorithm. Specifically, each time series has been obtained by running the program with a fixed time step of 1 ps.

References

1. Koyama, F. Recent advances of VCSEL photonics. *J. Lightw. Technol.* **24**, 4502–4513 (2006).
2. Michalzik, R. (Ed.) *VCSELs: fundamentals, technology and applications of vertical-cavity surface-emitting lasers* (Vol. 166). Springer (2012).
3. San Miguel, M., Feng, Q. & Moloney, J. V. Light-polarization dynamics in surface-emitting semiconductor lasers. *Phys. Rev. A* **52**, 1728 (1995).
4. Martin-Regalado, J., Prati, F., San Miguel, M. & Abraham, N. B. Polarization properties of vertical-cavity surface-emitting lasers. *IEEE J. Quantum Electron.* **33**, 765–783 (1997).
5. Sciamanna, M. *et al.* Optical feedback induces polarization mode hopping in vertical-cavity surface-emitting lasers. *Opt. Lett.* **28**, 1543–1545 (2003).
6. Hong, Y., Spencer, P. S. & Shore, K. A. Suppression of polarization switching in vertical-cavity surface-emitting lasers by use of optical feedback. *Opt. Lett.* **29**, 2151–2153 (2004).
7. Tabaka, A. *et al.* Dynamics of vertical-cavity surface-emitting lasers in the short external cavity regime: pulse packages and polarization mode competition. *Phys. Rev. A* **73**, 013810 (2006).

8. Zhang, W. L., Pan, W., Luo, B., Wang, M. Y. & Zou, X. H. Polarization switching and hysteresis of VCSELs with time-varying optical injection. *IEEE J. Sel. Top. Quantum Electron.* **14**, 889–894 (2008).
9. Sakaguchi, J., Katayama, T. & Kawaguchi, H. High switching-speed operation of optical memory based on polarization bistable vertical-cavity surface-emitting laser. *IEEE J. Quantum Electron.* **46**, 1526–1534 (2010).
10. Xiang, S. *et al*. Influence of polarization mode competition on chaotic unpredictability of vertical-cavity surface-emitting lasers with polarization-rotated optical feedback. *Opt. Lett.* **36**, 310–312 (2011).
11. Salvide, M. F., Torre, M. S., Henning, I. D., Adams, M. J. & Hurtado, A. Dynamics of normal and reverse polarization switching in 1550-nm VCSELs under single and double optical injection. *IEEE J. Sel. Top. Quantum Electron.* **21**, 643–651 (2015).
12. Jiang, B. *et al*. Polarization switching characteristics of 1550-nm vertical-cavity surface-emitting lasers subject to double polarization pulsed injection. *IEEE J. Quantum Electron.* **52**, 1–7 (2016).
13. Zhong, Z. Q. *et al*. Polarization dynamics of 1550-nm VCSELs subject to polarization-preserved FBGfeedback. *IEEE Photon. Tech. Lett.* **28**, 963–966 (2016).
14. Li, N., Susanto, H., Cemlyn, B. R., Henning, I. D. & Adams, M. J. Stability and bifurcation analysis of spin-polarized vertical-cavity surface-emitting lasers. *Phys. Rev. A* **96**, 013840 (2017).
15. Hurtado, A., Schires, K., Henning, I. D. & Adams, M. J. Investigation of vertical cavity surface emitting laser dynamics for neuromorphic photonic systems. *Appl. Phys. Lett.* **100**, 103703 (2012).
16. Nahmias, M. A., Shastri, B. J., Tait, A. N. & Prucnal, P. R. A leaky integrate-and-fire laser neuron for ultrafast cognitive computing. *IEEE J. Sel. Top. Quantum Electron.* **19**, 1–12 (2013).
17. Xiang, S., Wen, A. & Pan, W. Emulation of spiking response and spiking frequency property in VCSEL-based photonic neuron. *IEEE Photon. J.* **8**, 1–9 (2016).
18. Deng, T., Robertson, J. & Hurtado, A. Controlled propagation of spiking dynamics in vertical-cavity surface-emitting lasers: towards neuromorphic photonic networks. *IEEE J. Sel. Top. Quantum Electron.* **23**, 1–8 (2017).
19. Robertson, J., Deng, T., Javaloyes, J. & Hurtado, A. Controlled inhibition of spiking dynamics in VCSELs for neuromorphic photonics: theory and experiments. *Opt. Lett.* **42**, 1560–1563 (2017).
20. Xiang, S. Y. *et al*. Cascadable Neuron-Like Spiking Dynamics in coupled VCSELs subject to orthogonally polarized optical pulse injection. *IEEE J. Sel. Top. Quantum Electron.* **23**, 1–7 (2017).
21. Zhang, Y. *et al*. Spike encoding and storage properties in mutually coupled vertical-cavity surface-emitting lasers subject to optical pulse injection. *Appl. Optics* **57**, 1731 (2018).
22. Xiang, S., Zhang, Y., Guo, X., Wen, A. & Hao, Y. Photonic Generation of neuron-like dynamics using VCSELs subject to double polarized optical injection. *J. Lightw. Technol.* **36**, 4227–4232 (2018).
23. Philip, Y. M. *et al*. All-optical digital-to-spike conversion using a graphene excitable laser. *Opt. Express* **25**, 33504 (2017).
24. Barbay, S., Kuszelewicz, R. & Yacomotti, A. M. Excitability in a semiconductor laser with saturable absorber. *Opt. Lett.* **36**, 4476–8 (2011).
25. Yamada, M. A theoretical analysis of self-sustained pulsation phenomena in narrow-stripe semiconductor lasers. *IEEE J. Quantum Electron.* **29**, 1330–1336 (1993).
26. Scirè, A., Mulet, J., Mirasso, C. R. & San Miguel, M. Intensity and polarization self-pulsations in vertical-cavity surface-emitting lasers. *Opt. Lett.* **27**, 391–393 (2002).
27. Scire, A., Mulet, J., Mirasso, C. R., Danckaert, J. & San Miguel, M. Polarization message encoding through vectorial chaos synchronization in vertical-cavity surface-emitting lasers. *Phys. Rev. Lett.* **90**, 113901 (2003).
28. Selmi, F. *et al*. Relative refractory period in an excitable semiconductor laser. *Phys. Rev. Lett.* **112**, 183902 (2014).
29. Selmi, F. *et al*. Spike latency and response properties of an excitable micropillar laser. *Phys. Rev. E* **94**, 042219 (2016).
30. Ostojic, S. Two types of asynchronous activity in networks of excitatory and inhibitory spiking neurons. *Nat. Neurosci.* **17**, 594 (2014).
31. Kasturia, S., Aslanis, J. T. & Cioffi, J. M. Vector coding for partial response channels. *Milcom88 Oct* **2**, 741–762 (1990).

Acknowledgements

We would like to thank Dr. Jose Marques-Hueso, from Heriot-Watt University, for proofreading of the manuscript. We would also like to thank Dr. Tao Ma for the helpful writing advice. This work was supported in part by the National Natural Science Foundation of China under Grants 61674119, 61306061, and 61274042, in part by the National Postdoctoral Program For innovative Talents in China under Grant BX201600118, in part by the Young Talent fund of University Association for Science and Technology in Shaanxi, China, under Grants 20160109, in part by the China 111 project under Grant B08038, in part by Natural Science Basic Research Plan in Shaanxi Province of China under Grants 2017JM6002 and 2016JM6009, in part by the Fundamental Research Funds for the Central Universities, in part by the Innovation Fund of Xidian University under Grants JB182001.

Author Contributions

Shuiying Xiang, Aijun Wen and Yue Hao conceived and designed the study. Shuiying Xiang, Xingxing Guo and Yahui Zhang performed the theoretical study and numerical simulations. All authors analyzed the results and wrote the manuscript.

Additional Information

Competing Interests: The authors declare no competing interests.

Publisher's note: Springer Nature remains neutral with regard to jurisdictional claims in published maps and institutional affiliations.